Modeling and control of a Magnus effect-based airborne wind energy system in crosswind maneuvers

Yashank Gupta, Jonathan Dumon, Ahmad Hably

Modeling and control of a Magnus effect-based airborne wind energy system in crosswind maneuvers

Yashank Gupta * **Jonathan Dumon** * **Ahmad Hably** *

* *Univ. Grenoble Alpes, CNRS, GIPSA-Lab, F-38000 Grenoble, France (e-mail: ahmad.hably@gipsa-lab.grenoble-inp.fr).*

Abstract: In this paper, a 3-D model of a Magnus effect-based airborne wind energy system adapted from flight dynamics is proposed. The model is derived from first principles where the forces acting on the system are presented. In order to validate our aerodynamic model, a study of lift and drag coefficients is presented for the rotating cylinders in high Reynolds number regime. The proposed 3-D model is validated by simulation, controlling the system in crosswind trajectories. The performance of the system power production is also assessed and compared to a simplified static model.

Keywords: Airborne wind energy system, Magnus effect, modeling, control, crosswind trajectories, power production.

1. INTRODUCTION

Airborne wind energy (AWE) has attracted the attention of multi-disciplinary community of researchers and technologists during the last years [Cherubini et al. (2015)]. Their motivation is to overcome the limitation of conventional wind turbine, by using a controlled tethered airborne module that captures the energy of the wind. Different concepts have been proposed and they can be classified as a function of the location of energy production: On-board production and on-ground production.

For on-board production AWE systems, electrical energy is generated by means of one or more airborne generators and returned to the ground by conducting cables. One can cite the solutions proposed by Sky WindPower [Roberts et al. (2007)], Joby energy [Joby-Energy (2011)], Magenn Rotor System [Magenn (2012)], Altaeros Energies [Altaeros (2015)], and Makani Power who has passed the experimental phase with its prototype 600 kW [Makani-Power (2016)].

The second category of AWE system, on-ground production, consists of a wing or kite (flexible or rigid) attached to one or more cables and enrolled to the ground on a drum connected to the electric generator. Energy is produced by controlling the path of the wing to maximize the traction force. Indeed, the apparent wind on the wing is then the sum of the wind speed and kite speed, which maximizes the power generated per m^2 wing. This system allows for the aerial part to be light and the usage of conductive cable is avoided. There are several research groups and some companies have adopted this solution. For these systems one can cite e-kite [E-kite (2016)] and Enerkite that has already built a 30 kW demonstration embarked on a truck [Enerkite (2016)].

A Magnus effect-based system has been used by Omnidea Lda in its High Altitude Wind Energy project (HAWE) [Omnidea (2013)]. The operation principle of the platform is based on the traction force of a rotating cylindrical balloon employing both aerostatic as well as aerodynamic lift mechanisms [Penedo et al. (2013); Pardal and Silva (2015)]. The feasibility of the Magnus effect-based concept has been studied in [Perković et al. (2013)]. The authors of [Milutinović et al. (2015)] have optimized control variables for a Magnus effect-based AWE system showing optimal vertical trajectories. In our previous work [Hably et al. (2016)], we have proposed a strategy that controls the power produced by the system by changing the tether length and the cycle period. The movement of the Magnus effect-based AWE system ,hereafter, referred to as airborne module (ABM), is limited to the vertical plane.

In this paper, we introduce the governing equations of motion in the space describing the dynamic model of the Magnus effect-based AWE system. The current literature on ABM chiefly, discusses 2-D model [Milutinović et al. (2015), Hably et al. (2016)] to describe the ABM dynamics. However, there is no existing literature (to the best of our knowledge) presenting a 3-D model for the AWE systems based on Magnus effect. Hence, this present paper is our attempt to supplement the literature on AWE systems based mainly on Magnus effect. In addition, this model is used to implement feedback controllers that aim to obtain figure-eight crosswind flying paths such as the one proposed by Fagiano et al. (2014). This result (to the best of our knowledge) is the first contribution in the scientific literature on the control of Magnus effect-based AWE system in crosswind trajectories.

The paper is organized as follows. Section 2 describes the derivation of the model with a discussion on its drag and lift coefficients. In section 3, the proposed control strategy is presented. In Section 4, results of simulation and performance of the control strategy are presented. The paper ends with conclusions in Section 5.

2. SYSTEM MODELING

2.1 Magnus effect-based cylinder aerodynamic model

Magnus effect-based AWE system consists of a tethered airborne cylinder or rotor using the Magnus effect. The Magnus effect phenomenon was first defined by German scientist Gustav Magnus in 1852. His work established that spinning cylinders produce a force, similar to the lift force produced by airfoils when exposed to wind flow. The spin of the cylinder actually causes an unequal distribution of pressure at the top and the bottom of the cylinder, resulting in upward lift force. Due to the symmetry of the cylinder, Magnus effect-based AWE systems have an advantage over other such systems, as symmetry axis make them insensitive to the apparent wind direction, and thus, more robust with respect to wind gusts. On the other hand, it also has a lift coefficient much higher than that of conventional wings. The lift coefficient can be increased further by adding Thom discs to the cylinder [Thom et al. (1933)]. This allows the system to fly at much slower speeds for a given power and be less sensitive to the drag of the whole system. Lift and drag forces for the Magnus cylinder can be expressed by:

$$L = \frac{1}{2}\rho S_{cyl} v_a^2 C_L, \quad D = \frac{1}{2}\rho S_{cyl} v_a^2 C_D \tag{1}$$

where, v_a is the relative air flow on the wing, ρ is the air density, and S_{cyl} is the Magnus rotor projected surface area in the direction of the apparent wind velocity. C_L and C_D are respectively the lift and drag coefficients. These coefficients are primarily the result of the spin ratio X and shape contrary to the airfoils where C_L and C_D are primarily the result of its angle of attack and shape. The spin ratio X is defined with the following expression:

$$X = \frac{\omega_{cyl} r_{cyl}}{v_a} \tag{2}$$

where, r_{cyl} is the radius of the Magnus rotor and ω_{cyl} the Magnus rotor angular velocity. Another parameter that influences these coefficients is Reynolds number (Re). When rotating in the air flow, a torque acts around the axis of rotation of the cylinder that is usually expressed (for example in [Da-Qing et al. (2012),Seifert (2012) and Karabelas et al. (2012)]) as following:

$$T_{motor} = \frac{1}{2}\rho S_{cyl} V^2 2 r_{cyl} C_m \tag{3}$$

where, C_m is the torque coefficient that depends mainly on spin ratio X, geometry of the cylinder, roughness of its surface and Reynolds number. This torque has to be produced by an embedded motor in order to rotate the cylinder. This part of the system is out of the scope of this paper.

In order to establish a control oriented mathematical model for the ABM module, determination of respective aerodynamic coefficients C_L and C_D is a necessary step. This requires the study of flow past rotating cylinders in high Reynolds number regime as our operating Reynolds number lies between the range of Re from $5e5$ to $1e7$, and the spin ratio is between $[0, 6]$. However, there is a lack of published data dealing with rotating cylinders in high Reynolds number regime, primarily, because of the lack of interest of fluid dynamicists, and secondly, due to the high complexity of the problem. As a comprehensive CFD study of the ABM is beyond the scope of our work, in order to establish a good approximation of C_L and C_D, we undertook a brief study of some prominent research papers on rotating cylinders in high Reynolds number regime, to establish a general trend for C_L and C_D.

Figures 1 and 2, and Table 1 present a selection of aerodynamic data on C_L and C_D for high Re number range [Milutinović et al. (2015), Reid (1924), Borg (1986), Bergeson et al. (1974), **?**, Badalamenti and Prince (2008)]. The general trend for C_L can be assumed to be increasing linearly with spin ratio until the maximum value. Depending upon the aspect ratio of the cylinder, and the presence of Thom discs or not, $C_{L,max}$ can be between 8 to 14. Unlike the C_L curves, C_D curves are more scattered which can be attributed to a higher sensitivity to parameters like Thom disc presence and aspect ratio. Based on this analysis, we can conclude that the aerodynamic model proposed by Milutinović et al. (2015), for a Magnus cylinder with low aspect ratio, and expressed by the following equations :

$$C_D = -0.0211X^3 + 0.1873X^2 + 0.1183X + 0.5 \tag{4}$$

$$C_L = 0.0126X^4 - 0.2004X^3 + 0.7482X^2 + 1.3447X \tag{5}$$

is somewhat in line with the other presented experimental data.Thereupon, can be considered as an average model representing C_L and C_D values for the considered Re number range. Nevertheless, this aerodynamic model can be improved further in future works.

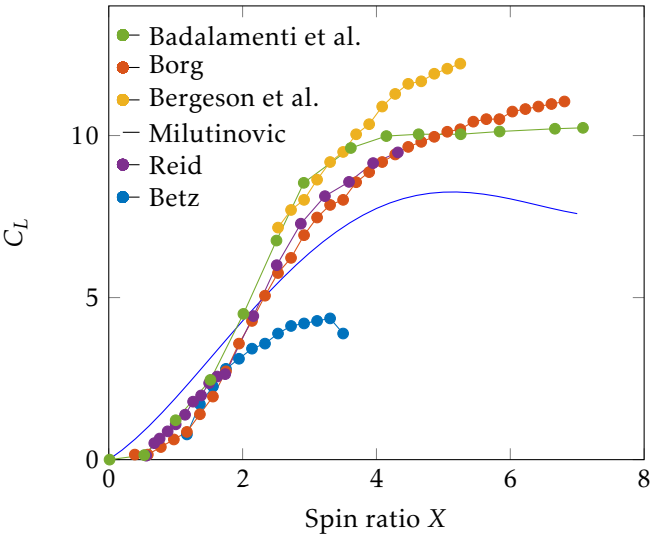

Fig. 1. The lift coefficient C_L as a function of X in several studies with different Reynolds number.

2.2 System Model

Several approaches are used to describe the dynamics of Kite-based AWE systems. One approach as stated in [Jehle and Schmehl (2014)] is to model the system in the earth centered earth fixed (ECEF) frame, describing the direction of the wind, and use a second (North-east-down) NED frame to describe the location of the ground station, and a third body fixed frame describing the dynamics of the Kite with respect to the ground station. In another approach, described in [Williams et al. (2008)], the attitude of kite and its position are decoupled by developing separate equation of motion for the bridle point in an inertial frame fixed at the ground station. A second frame is assumed to be fixed at the bridle point and a third body fixed frame is used to describe the attitude of the kite with respect to bridle point. Several other similar models using simple equations can be found in [Costello et al. (2015); Fagiano et al. (2014); Loyd (1980)]. Such approaches are highly useful

Reference	Re	AR	Data Type	Comments
Betz (1925)	5.2e4	4.7	Experimental	Without Thom disc
Borg (1986)	1.115e5	4	Experimental	Without Thom disc
Bergeson et al. (1974)	4.5e5		Experimental	With Thom discs
Reid (1924)	5e4	13.3	Experimental	Without Thom discs
Milutinović et al. (2015)	3.8e4	-	Identified.	From White (2003)
Badalamenti and Prince (2008)	9.5e4	5.1	Experimental	With endplates

Table 1. Different references used in the study of C_L and C_D. Aspect ratio AR and Reynolds number Re are given.

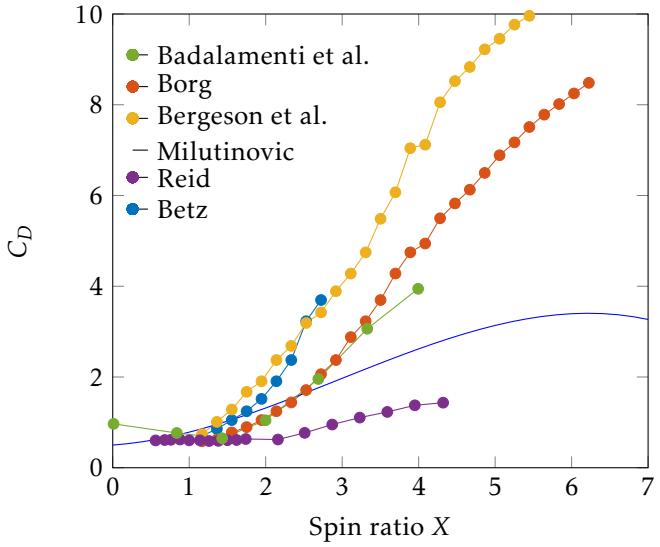

Fig. 2. The drag coefficient C_D as a function of X in several studies with different Reynolds number.

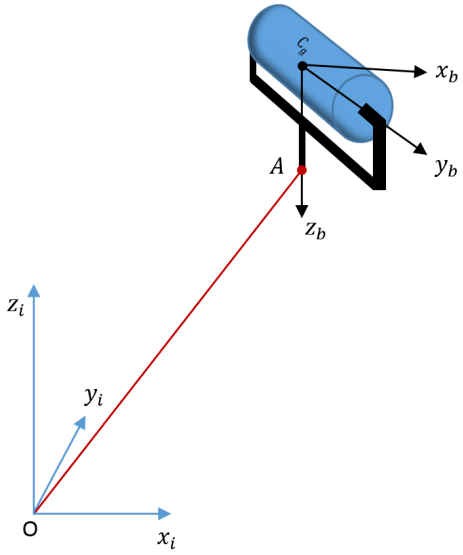

Fig. 3. Magnus Model and the frames.

in describing the dynamics of kite as the kite systems are a non-rigid structure consisting of a complex bridle system, often with multiple lines used to steer the system.

In our formulation, we consider a Magnus cylinder, consisting of a single tether, with the cylinder mounted on a rigid frame, free to rotate on its own axis. The frame is connected to ground based generator through the tether and the force developed in the tether is used to drive the winch located at origin O. We neglect the dynamics of the bridle point and describe the dynamics of the ABM with respect to an inertial frame fixed at the ground station. We also, neglect the tether elasticity, its inertia, and its aerodynamic drag. Figure 3 presents an illustration of the Mangus AWE model. The position of the ABM is described with respect to an inertial frame, x_i, y_i, z_i fixed at the ground station. Wind is assumed to be in the x_i direction. The attitude of the ABM is described with respect to body frame x_b, y_b, z_b centered at the centre of gravity C_g of the ABM system, which is assumed to coincide with the geometrical center of the Magnus cylinder. The cylinder is free to rotate around its own axis aligned with y_b. Point A represents the bridle point where the tether is attached to the rigid structure on which the Magnus cylinder is mounted, shifted from C_g along z_b axis. Using the sign conventions from flight dynamics, the body frame is assumed to be in the North-east-down direction (NED), and the attitude of ABM is described using Euler angles, ψ, θ, and ϕ defined with intrinsic ZYX convention.

2.3 Rotation matrices

The transformation of the inertial frame into the body frame is carried out by the standard ZYX transformation using rotation matrices, R_b^i .i.e. by rotating around $\boldsymbol{z}_i$ by ψ, followed by a second rotation around $\boldsymbol{y}_1$ by θ, and finally by ϕ around $\boldsymbol{x}_2$. In addition to this, we use another matrix L_{flip} to flip the coordinate system to align it with the NED frame.

$$\boldsymbol{\Theta} = \psi \boldsymbol{z}_i + \theta \boldsymbol{y}_1 + \phi \boldsymbol{x}_2 \tag{6}$$

$$R_b^i = \begin{bmatrix} c_\theta c_\psi & c_\theta s_\psi & -s_\theta \\ s_\phi s_\theta c_\psi - c_\phi s_\psi & s_\phi s_\theta s_\psi + c_\phi c_\psi & s_\phi c_\theta \\ c_\phi s_\theta c_\psi + s_\phi s_\psi & c_\phi s_\theta s_\psi - s_\phi & s_\psi \; c_\phi c_\theta \end{bmatrix} \tag{7}$$

where, "s" and "c" denote sine and cosine functions.

$$L_{flip} = \begin{bmatrix} 1 & 0 & 0 \\ 0 & -1 & 0 \\ 0 & 0 & -1 \end{bmatrix} \tag{8}$$

2.4 Equation of Motion

Assuming the Magnus cylinder as a rigid cylinder, the position of the C_g of the cylinder can be presented by a position vector in inertial frame $\boldsymbol{r_i}$,

$$\boldsymbol{r_i} = x\boldsymbol{x}_i + y\boldsymbol{y}_i + z\boldsymbol{z}_i \tag{9}$$

where, $\boldsymbol{x}_i, \boldsymbol{y}_i$, and $\boldsymbol{z}_i$ represent the unit vectors in the inertial frame. Hence,

$$\boldsymbol{r_b} = R_b^i L_{flip} \boldsymbol{r_i} \tag{10}$$

with $\boldsymbol{r_b}$ representing the position vector of the ABM in body frame. The translational velocity of the C_g is given by:

$$\dot{\boldsymbol{r_i}} = \boldsymbol{v_i} \tag{11}$$

Applying the axis transformation, the body frame velocity of the ABM is expressed by:

$$\boldsymbol{v_b} = R_b^i L_{flip} \boldsymbol{v_i} \tag{12}$$

Hence, equation of translation of C_g w.r.t inertial frame is given by :

$$\dot{r_i} = (L_{flip})^{-1} (R_b^i)^{-1} v_b \tag{13}$$

The attitude of the ABM is described using Euler angles ψ, θ, and ϕ defined with intrinsic ZYX convention. As in flight dynamics, the angular rates are measured about respective axis of rotation, i.e. $\boldsymbol{z}_i$, $\boldsymbol{y}_1$, and $\boldsymbol{x}_2$. Therefore,

$$\dot{\Theta}_b = \dot{\psi}\boldsymbol{z}_i + \dot{\theta}\boldsymbol{y}_1 + \dot{\phi}\boldsymbol{x}_2 \tag{14}$$

Expressing $\boldsymbol{z}_i$ and $\boldsymbol{y}_1$ with respect to $\boldsymbol{x}_b$, $\boldsymbol{z}_b$, and $\boldsymbol{y}_b$, we obtain:

$$\begin{bmatrix} p \\ q \\ r \end{bmatrix} = W_i \begin{bmatrix} \dot{\phi} \\ \dot{\theta} \\ \dot{\psi} \end{bmatrix} \tag{15}$$

with

$$W_i = \begin{bmatrix} 1 & 0 & -\sin\theta \\ 0 & \cos\phi & \sin\phi\cos\theta \\ 0 & -\sin\phi & \cos\phi\cos\theta \end{bmatrix} \tag{16}$$

and p, q,and r represents the respective angular rates in body frame. As a result, the equation for rate of change of angular position is

$$\dot{\Theta} = W_i^{-1} \tilde{\omega}_b \tag{17}$$

with

$$\tilde{\omega}_b = \begin{bmatrix} p \\ q \\ r \end{bmatrix} \tag{18}$$

For the simplicity purpose, we assume that the center of pressure coincides with the center of gravity. Applying Newton's second law of motion to the ABM and using Coriolis theorem, the equation of rate of change of translational velocity in body frame is given by:

$$\dot{\boldsymbol{v}}_b = \frac{1}{m}(\boldsymbol{F_b} - \tilde{\omega}\boldsymbol{v_b}) \tag{19}$$

where,

$$\tilde{\omega} = \begin{bmatrix} 0 & -r & q \\ r & 0 & -p \\ -q & p & 0 \end{bmatrix} \tag{20}$$

and F_b is the total body forces acting on the ABM expressed in body frame, and is given by:

$$\boldsymbol{F_b} = \boldsymbol{F_L} + \boldsymbol{F_D} + \boldsymbol{F_{dy}} + \boldsymbol{W_b} + \boldsymbol{F_{bu}} + \boldsymbol{F_r} \tag{21}$$

$\boldsymbol{F_L}$ and $\boldsymbol{F_D}$ are respectively the lift and drag force due to Magnus effect expressed in $x_b z_b$ plane, $\boldsymbol{F_{dy}}$ is the drag force acting on the ABM in y_b direction, and $\boldsymbol{F_r}$ is the tether force applied from the ground station. $\boldsymbol{W_b}$ and $\boldsymbol{F_{bu}}$ are respectively weight and buoyancy forces acting on the ABM in opposite direction. All these forces illustrated in Fig.4 are expressed in body frame.

Since, the weight of the ABM and the buoyancy force are acting in the z_i direction, rotational matrices are used to express them in the body frame.

$$\boldsymbol{g_b} = R_b^i L_{flip} \begin{bmatrix} 0 \\ 0 \\ -g \end{bmatrix} \tag{22}$$

$$\boldsymbol{W_b} = m\boldsymbol{g_b} \tag{23}$$

$$\boldsymbol{F_{bu}} = -\rho r_{cyl}^2 \pi l_{cyl} \boldsymbol{g_b} \tag{24}$$

where, r_{cyl} and l_{cyl} are the radius and the length of the Magnus rotor respectively, g is the gravitational constant and m is the total mass of the ABM .i.e. the sum of the mass of the structure m_{struct} and the mass of the Magnus rotor filled a gas of density ρ_{gaz}:

$$m = m_{struct} + \rho_{gaz} r_{cyl}^2 \pi l_{cyl} \tag{25}$$

Aerodynamic forces, $\boldsymbol{F_L}$, $\boldsymbol{F_D}$, and $\boldsymbol{F_{dy}}$ are then evaluated as following:

$$\boldsymbol{F_L} = \frac{1}{2}\rho S_{cyl} v_{axz}^2 C_L \boldsymbol{e_{Fl}} \tag{26}$$

$$\boldsymbol{F_D} = \frac{1}{2}\rho S_{cyl} v_{axz}^2 C_D \boldsymbol{e_{Fd}} \tag{27}$$

$$\boldsymbol{F_{dy}} = \frac{1}{2}\rho S_{cyl} v_{ay}^2 C_{dy} \boldsymbol{y_b} \tag{28}$$

where, $S_{cyl} = 2 r_{cyl} l_{cyl}$ and C_{dy} is the drag coefficient of the ABM along $\boldsymbol{y_b}$ axis. Apparent wind velocity $\boldsymbol{v_a}$ is decomposed in a $\boldsymbol{y_b}$ component and the remaining ($\boldsymbol{x_b z_b}$) component, expressed in the body frame:

$$\boldsymbol{v_a} = \boldsymbol{v_w} - \boldsymbol{v_b} \tag{29}$$

$$\boldsymbol{v_{axz}} = \boldsymbol{v_a}. \begin{bmatrix} 1 \\ 0 \\ 1 \end{bmatrix} = v_{axz} \boldsymbol{e_{Fl}} \tag{30}$$

$$\boldsymbol{v_{ay}} = \boldsymbol{v_a}. \begin{bmatrix} 0 \\ 1 \\ 0 \end{bmatrix} = v_{ay} \boldsymbol{y_b} \tag{31}$$

where, "." is an element-wise product operator, $\boldsymbol{e_{Fl}}$ and $\boldsymbol{y_b}$ are unit vectors, $\boldsymbol{v_w}$ is the wind velocity expressed in body frame and $\boldsymbol{v_b}$ is the translational velocity of the ABM.
The tether force $\boldsymbol{F_r}$ is then evaluated from the dynamic model of the winch:

$$\frac{J_z}{R}\ddot{r}_t = RF_r + T_c \tag{32}$$

where, J_z is the moment of inertia of the winch, R is its radius and T_c is the torque produced by the electric actuator. The length of the tether is given by $r_t = \sqrt{(x^2 + y^2 + z^2)}$ and F_r represents the norm of the tether force applied on the ABM,

$$F_r = \frac{J_z}{R^2}\ddot{r}_t - \frac{T_c}{R} \tag{33}$$

As $\boldsymbol{F_r}$ is evaluated at the ground station in the tether direction, it is expressed in body frame by following expression:

$$\boldsymbol{F_r} = F_r R_b^i L_{flip} \frac{\boldsymbol{r_i}}{\|\boldsymbol{r_i}\|} \tag{34}$$

Finally, winch torque T_c is controlled by the reference variable u_T and acts on the electrical torque through a current loop modeled by a first order dynamic system:

$$\dot{T_c} = \beta_T (u_T - T_c) \tag{35}$$

where β_T, homogeneous to a frequency, represents its dynamic response. Similarly, the equation for the rate of change of angular velocity is obtained by applying Newton's second law:

$$\dot{\omega} = I^{-1}(M_b - \tilde{\omega} I \omega) \tag{36}$$

where, I represents the moment of inertia matrix and M_b is the sum of all torques acting on the ABM expressed in the body frame. As the bridle point A, where $\boldsymbol{F_r}$ is applied, is shifted along $\boldsymbol{z_b}$ from C_g where acts other forces, the ABM will naturally self-align to the tether. This results into the alignment of the 3 points O, A and C_g, and $\boldsymbol{z_b}$ will be parallel to the tether. The remaining free rotation is around the axis $\boldsymbol{z_b}$ which corresponds to γ, the yaw angle of the ABM. For the sake of simplicity, modeling of this dynamics is not considered, and

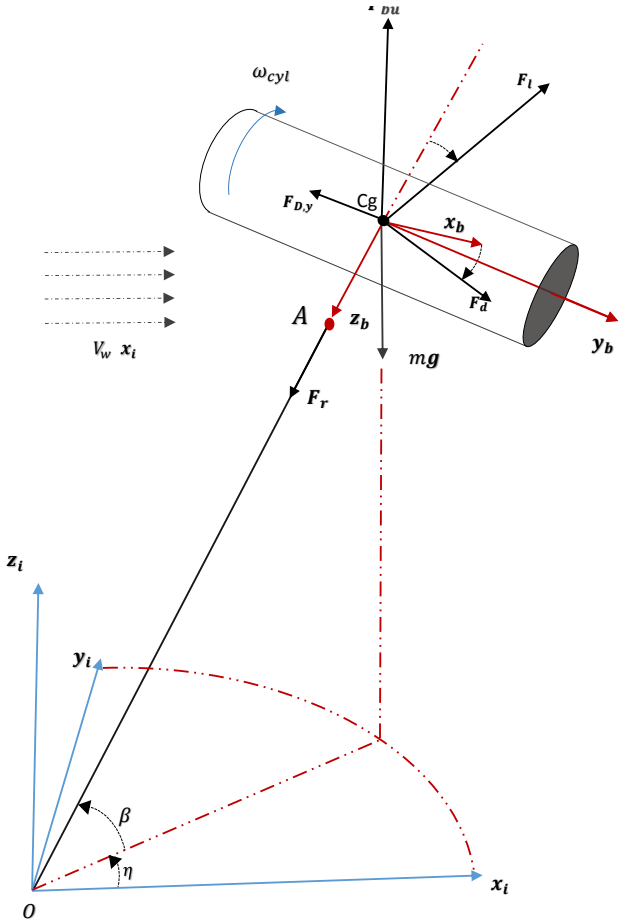

Fig. 4. The forces acting on the Magnus rotor.

will be a part of the future work. We assume here that the self-alignment is done smoothly and significantly faster than other considered dynamics in order to neglect it. We also assume that an appropriate actuator, like a suitably sized rudder, is used to steer the ABM to the desired yaw γ_{ref}. In simulations subsequently presented (Sect. 4), $\boldsymbol{z_b}$ is forced in the direction of the origin, and the last free rotation γ around $\boldsymbol{z_b}$ axis follows the reference γ_{ref} through a first order dynamic system:

$$\dot{\gamma} = \beta_\gamma(\gamma_{ref} - \gamma) \tag{37}$$

where β_γ, homogeneous to a frequency, represents its dynamic response. Finally, a control loop on cylinder speed of rotation is also assumed to be set properly and is modeled by a first order dynamic system:

$$\dot{\omega}_{cyl} = \beta_{\omega_{cyl}}(\omega_{cyl_{ref}} - \omega_{cyl}) \tag{38}$$

where $\beta_{\omega_{cyl}}$, homogeneous to a frequency, represents its dynamic response.

3. CONTROL STRATEGY

3.1 Global control of the cycle

During the cycle, the Magnus rotor moves from a minimum radial position r_{min} to a maximum radial position r_{max} at a reel-out speed $\dot{r}_{prod}$ during production phase, and from r_{max} to r_{min} at a negative reel-in speed $\dot{r}_{rec}$ during the recovery phase. A given cycle is defined by the time period from the beginning of the production phase to the end of the recovery phase. The production phase starts at time t_0 and ends at time t_1. The recovery phase starts at time t_1 and ends at time t_2. Time t_1 is calculated by

$$t_1 = t_0 + \frac{(r_{max} - r_{min})}{\dot{r}_{prod}} \tag{39}$$

Time t_2 is calculated by

$$t_2 = t_1 + \frac{(r_{max} - r_{min})}{\dot{r}_{rec}} \tag{40}$$

During the production phase, spin ratio X_{max} is used for the Magnus rotor while it is following figure-eight trajectories through the control of yaw angle γ in order to maximize the power produced. The guidance strategy is similar to that proposed by [Fagiano et al. (2014)], detailed in Sect.3.2. During the recovery phase, yaw angle γ is set to zero while fixing the spin ratio to its minimum X_{min} in order to minimize the power consumed during this phase. The radial speeds for production and recovery phases are set to be constant in order to maximize the total net power produced of the system. The output power P_g of the on-ground generator is calculated by:

$$P_g = \dot{r}_t \frac{T_c}{R} \tag{41}$$

A PID control K_1 is used in order to follow the radial position $r_{t_{ref}}$ through the control variable u_T acting on the winch actuator. The response time for this control loop is set to be faster than variations than other forces in order to get an efficient production cycle. An overview of control strategy is presented in Fig.5.

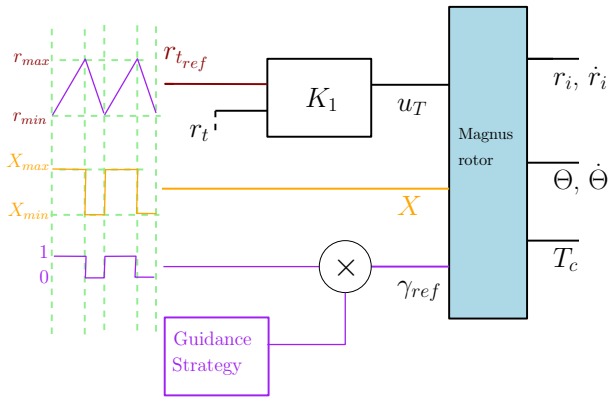

Fig. 5. An overview of the control strategy. The Magnus rotor moves from minimum radial position r_{min} to a maximum radial position r_{max}.

3.2 Guidance strategy

Two reference points denoted by $P_- = (\beta_-, \eta_-)$ and $P_+ = (\beta_+, \eta_+)$ (Fig.6 from [Fagiano et al. (2014)]). We set the reference angles to the same value $\beta_+ = \beta_- = \beta_{ref}$ and $\eta_+ = -\eta_- = \eta_{ref}$. At each time instant, one of the two reference points is set as the active target P_T, according to a switching strategy. γ_{ref} is computed on the basis of the measured values of β and η by

$$\gamma_{ref} = -\arctan\left(\frac{(\beta_{ref} - \beta)\sin(\eta)}{\eta_T - \eta}\right) \tag{42}$$

The target points are chosen according to the following strategy:

$$\begin{cases} \text{If } \eta(t) < \eta_- & \text{then } P_T = P_+ \\ \text{If } \eta(t) > \eta_+ & \text{then } P_T = P_- \\ \text{else} & P_T(t) = P_T(t-1) \end{cases} \tag{43}$$

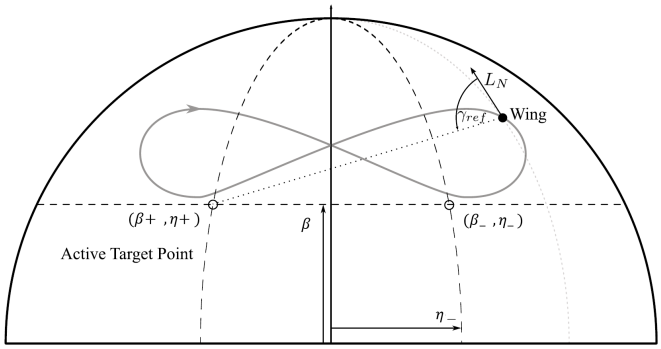

Fig. 6. Sketch of the guidance strategy borrowed from [Fagiano et al. (2014)].

Thus, the target point is switched when the measured value of η is outside the interval $[\eta_-, \eta_+]$.

Finally, in order to get figure-eight trajectories of the same width for all tether length for the production to be more stable, we set η_{ref} as a function of tether length r_t:

$$\eta_{ref} = \frac{k_\eta}{r_t} \tag{44}$$

with k_η is a coefficient for azimuth angle reference. The same approach can also be done for β_{ref} but was not used in this paper.

4. RESULTS

In this section, we first present a simplified model under the static assumption of the system presented in Sect.2 with the control strategy presented in Sect.3. It is used to set some of the parameters of the control strategy. We will then present the results of 3-D dynamic simulation for an hypothetical MW-sized Magnus effect-based AWE system. Results are finally compared with that of the simplified model under static assumption.

4.1 Performance under static assumptions

In the frame of equilibrium motion theory, the power that can be generated with a tethered airfoil in crosswind conditions has been set by Loyd (1980) and refined in Argatov et al. (2009) to take into consideration the β losses:

$$P_{prod} = \frac{1}{2}\rho\frac{4}{27}S_{cyl}(v_w\cos(\beta))^3 C_L\left(\frac{C_L}{C_D}\right)^2 \tag{45}$$

One way to maximize this power is to maximize the ratio $C_L\left(\frac{C_L}{C_D}\right)^2$. In addition, one has to set the unwinding speed of tether during the production phase $\dot{r}_{prod} = v_w/3$. For the considered Magnus rotor model, the maximum of $C_L\left(\frac{C_L}{C_D}\right)^2$ is found for $X = 3.6$ and is equal to 69.44. The power consumed can be calculated as the product of the winding speed of the tether $\dot{r}_{rec}$ and the resulting drag force of the Magnus rotor:

$$P_{rec} = \frac{1}{2}\rho S_{cyl}(v_w\cos(\beta) + \dot{r}_{rec})^2 C_{Drec}\dot{r}_{rec} \tag{46}$$

where, C_{Drec} is the drag coefficient during the recovery phase. In order to get a minimal power consumption during this phase, one has to set C_L to 0 and C_D to its minimal value C_{Drec}. For this, the speed of rotation ω is set to 0 during the recovery phase in order to make $C_L = 0$. Without considering the transition phases, the full production cycle of the Magnus rotor can then be computed by:

$$P_{cycle} = \frac{P_{prod}\dot{r}_{rec} - P_{rec}\dot{r}_{prod}}{\dot{r}_{rec} + \dot{r}_{prod}} \tag{47}$$

Note that there is a trade-off with $\dot{r}_{rec}$ because its augmentation not only increase the contribution of the production phase to the full production cycle, but also increases the power consumption P_{rec}.

4.2 Simulation parameters

The control strategy is applied on $500m^2$ Magnus effect-based AWE system with the parameters given in Table 2.
Dynamics of winch current loop β_T has been neglected in these results as it is much faster than all other dynamics considered in the simulation. On the other hand, we set a maximum value of its torque $T_{c_{max}}$ in order to evaluate the impact on the control strategy. Secondly, in order to smooth respectively peaks of tension in the tether and yaw movements, a second order filter has been applied on $r_{t_{ref}}$ and γ_{ref}. Thirdly, it is important to note that as F_r is transmitted through a tether, it has to be always negative. So F_r is set between $-\infty$ and 0 in order to simulate this physical constraint. Finally, PID controller K_1 parameters are $K_p = 5e7$ N, $K_i = 0.02$ N/s, $K_d = 0.2$ Ns and has been set empirically.

	Variable	Value
Air density $[kg/m^3]$	ρ	1.225
Gravitational constant $[m/s^2]$	g	9.81
Span of cylinder [m]	l_{cyl}	40
Radius of cylinder [m]	r_{cyl}	6.25
Aspect ratio	AR	3.2
Mass of airborne module [kg]	m_{struct}	6347
Radius of winch's drum [m]	R	2
Maximum winch actuator's torque [Nm]	$T_{c_{max}}$	4e6
Dynamic of speed of rotation loop [Hz]	$\beta_{\omega_{cyl}}$	1.43
Dynamic of yaw loop [Hz]	β_γ	1
Wind-speed, along $\boldsymbol{x_i}$ [m/s]	v_w	10
ABM lateral drag coefficient	C_{dy}	1.05
Maximum $C_L\left(\frac{C_L}{C_D}\right)^2$ for $X = 3.6$	$\max(C_L\left(\frac{C_L}{C_D}\right)^2)$	69.44
Reynolds number for $V = 10m/s$	Re	8.01e6
Minimum radial position [m]	r_{min}	150
Maximum radial position [m]	r_{max}	300
Reel-out speed [m/s]	$\dot{r}_{prod}$	3.3
Reel-in speed [m/s]	$\dot{r}_{rec}$	13.2
Spin ratio for production phase	X_{max}	3.6
Spin ratio for recovery phase	X_{min}	0.05
Reference for elevation angle [rad]	β_{ref}	0.436
Coefficient for azimuth angle ref. [rad.m]	k_η	13.09

Table 2. Parameters of the $500m^2$ Magnus effect-based AWE system and the simulation parameters.

4.3 Simulation results

In this subsection, we present simulation results for 3 consecutive cycles. Figure 7 shows the 3-D trajectory of the ABM both in the xz plane and yz plane. As it can be seen that the trajectory is stable as the 3 cycles are overlapping perfectly. In xz plane, it can be seen the control of figure-eight trajectory with fixed

elevation angle reference β_{ref}. Trajectory of the recovery phase starts to go up because the cylinder takes time to go from X_{max} to X_{min}. Then ABM goes down when X_{min} is reached. yz plane presents the constant width of figure-eight trajectory that keeps the covered area constant all over the production phase.

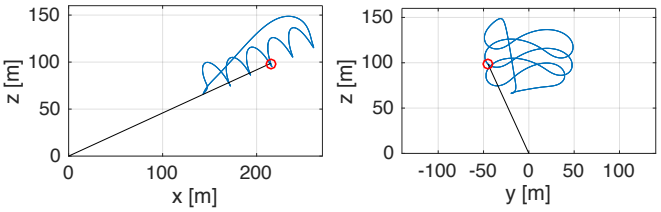

Fig. 7. Trajectories of the Magnus rotor in xz and yz planes for the 3 cycles.

In Fig.8 the main variables of the system are presented. The tether length r_t and its reference are overlapping perfectly thanks to the controller K_1 despite the saturation of the winch actuator. The tether tension curve shows this saturation at the beginning of each production phase. Evolution of speed of rotation shows that the system can follow the variations of apparent wind speed by adapting ω_{cyl} in order to keep spin ratio $X = X_{max}$. Finally, evolution of yaw variables gives also an idea of what type of control performance is needed in order to perform figure-eight trajectories with Magnus effect-based AWE system.

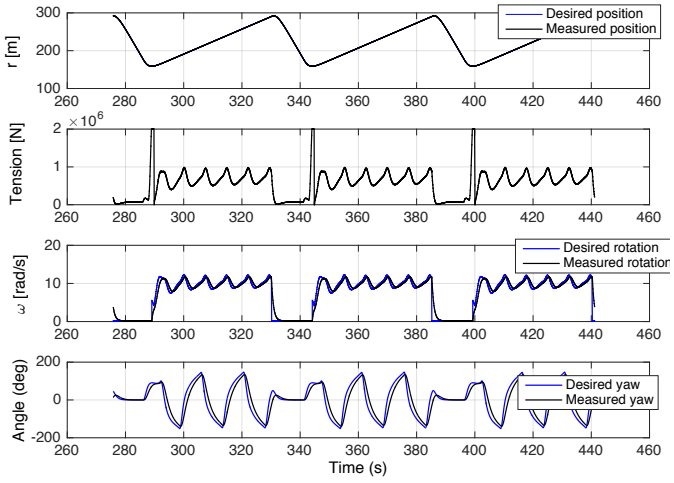

Fig. 8. Reference and state variable for tether length $(r_t, r_{t_{ref}})$, tether tension F_r, angular speed of the Magnus rotor $(\omega_{cyl}, \omega_{cyl_{ref}})$, and yaw angle (γ, γ_{ref}), as function of time for the 3 cycles.

In Fig.9, evolution of output power P_g is shown. The minimum value is -1.9MW and maximum is 3.9MW. This results in a mean power of the full cycle of 1.47MW. Note that embedded motor consumption to rotate the Magnus cylinder has to be subtracted from this value in order to have the total net power produced. This has to be done a in future work. Simplified model under static assumptions is also shown and is close to the mean of P_g dynamically simulated. The total mean power for simplified model $P_{cycle} = 1.67MW$, which is only 14% more. One can note that in order to produce around 1.5 MW of nominal power for $10m/s$ wind and this set of parameters, the generator has to be able to produce $4e6$ Nm torque and 6.6rad/s of rotation speed. This leads to a $26.6MW$ generator. A trade-off has then probably to be found in order to use a reasonable size of generator for the on-ground station. As these 2 extreme values are not needed in the same time, a gear box can also be considered. A 3.9 MW generator is then needed instead. Finally, the maximum torque can also be more limited, but a degradation of tether length control will occur.

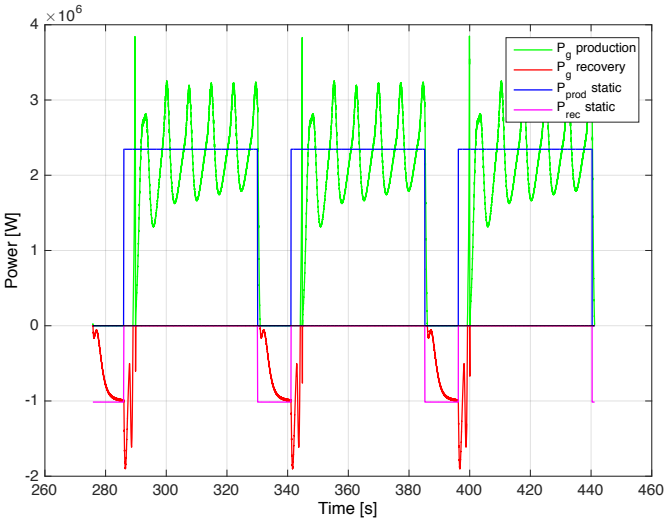

Fig. 9. The output power simulated P_g during production and recovery phases for the 3 cycles with a comparison with simplified model under static assumption. The mean output power is 1469 kW for dynamic simulation and 1674 kW for the simplified model.

5. CONCLUSIONS

We have presented modeling of various aspects of a Magnus effect-based AWE systems, that takes into account both the translational and rotational motion of the system. A brief study of the aerodynamic properties of the Magnus effect has been presented to provide an approximation of the aerodynamic properties of a Magnus model. Simulated results of the dynamic model of the system using bang-bang control strategy has been presented. With the assumption of the controllability of yaw angle of the system, it has been shown that the Magnus effect-based AWE systems can perform crosswind maneuvers. The results of static model have been found to be satisfactory and gives results close to the performance of the 3-D dynamic simulation. This modeling can be adapted to any on-ground production AWE system.

ACKNOWLEDGEMENTS

The authors would like to thank Garrett Smith at Wind Fisher for technical discussions.

REFERENCES

Altaeros (2015). http://www.altaerosenergies.com.

Argatov, I., Rautakorpi, P., and Silvennoinen, R. (2009). Estimation of the mechanical energy output of the kite wind generator. *Renewable Energy*, 34, 1525–1532.

Badalamenti, C. and Prince, S. (2008). The effects of endplates on a rotating cylinder in cross flow. In *26th AIAA Applied Aerodynamics Conf., Honolulu, Hawaii*.

Bergeson, L., Greenwald, C., and Hanson, T. (1974). Magnus rotor test and evaluation for auxiliary propulsion. *The Ancient Interface*, 13, 125.

Betz, A. (1925). Der magnuseffekt, die grundlage der flettnerwalze. *Zeitschrift des vereins deutscher Ingenieure. Translated to: the Magnus Effect The Principle of the Flettner rotor. NACA Technical Memorandum, TM-310*, 9–14.

Borg, J. (1986). The magnus effect-an overview of its past and future practical applications. *The Borg/Luther Group, Naval Sea Systems Command Contract*, (00024).

Cherubini, A., Papini, A., Vertechy, R., and Fontana, M. (2015). Airborne wind energy systems: A review of the technologies. *Renewable and Sustainable Energy Reviews*, 51, 1461–1476. doi:10.1016/j.rser.2015.07.053.

Costello, S., François, G., and Bonvin, D. (2015). Directional real-time optimization applied to a kite-control simulation benchmark. In *Control Conference (ECC), 2015 European*, 1594–1601. IEEE.

Da-Qing, L., Leer-Andersen, M., and Allenstrom, B. (2012). Performance and vortex formation of flettner rotors at high reynolds numbers. *The 29th Symposium on Naval Hydrodynamics Gothenburg, Sweden*.

E-kite (2016). http://www.e-kite.com.

Enerkite (2016). http://www.enerkite.de/en/products.

Fagiano, L., Zgraggen, A.U., Morari, M., and Khammash, M. (2014). Automatic crosswind flight of tethered wings for airborne wind energy:modeling, control design and experimental results. *IEEE Transactions on Control System Technology*, 22(4), 1433–1447. doi:10.1109/TCST.2013.2279592.

Hably, A., Dumon, J., and Smith, G. (2016). Control of an airborne wind energy system with a Magnus effect. In *The 2016 American Control Conference*. Boston, United States. URL `https://hal.archives-ouvertes.fr/hal-01272253`.

Jehle, C. and Schmehl, R. (2014). Applied tracking control for kite power systems. *JOURNAL OF GUIDANCE, CONTROL, AND DYNAMICS*, 37(4).

Joby-Energy (2011). http://www.jobyenergy.com/.

Karabelas, S., Koumroglou, B., Argyropoulos, C., and Markatos, N. (2012). High reynolds number turbulent flow past a rotating cylinder. *Applied Mathematical Modelling*, 36(1), 379–398.

Loyd, M.L. (1980). Crosswind kite power. *Journal of Energy*, 4(3), 106–111. doi:10.2514/3.48021.

Magenn (2012). http://www.magenn.com/.

Makani-Power (2016). https://www.solveforx.com/makani/.

Milutinović, M., Čorić, M., and Deur, J. (2015). Operating cycle optimization for a magnus effect-based airborne wind energy system. *Energy Conversion and Management*, 90, 154–165. doi:10.1016/j.enconman.2014.10.066.

Omnidea (2013). http://www.omnidea.net/hawe/.

Pardal, T. and Silva, P. (2015). Analysis of experimental data of a hybrid system exploiting the magnus effect for energy from high altitude wind. In *Book of Abstracts of the International Airborne Wind Energy Conference 2015*.

Penedo, R.J.M., Pardal, T.C.D., Silva, P.M.M.S., Fernandes, N.M., and Fernandes, T.R.C. (2013). High altitude wind energy from a hybrid lighter-than-air platform using the magnus effect. In *Airborne Wind Energy*.

Perković, L., Silva, P., Ban, M., Kranjčević, N., and Duić, N. (2013). Harvesting high altitude wind energy for power production: The concept based on magnus effect. *Applied Energy*, 101, 151–160. doi:10.1016/j.apenergy.2012.06.061.

Reid, E.G. (1924). Tests of rotating cylinders. *NACA TN*.

Roberts, B.W., Shepard, D.H., Caldeira, K., Cannon, M.E., Eccles, D.G., Grenier, A.J., and Freidin, J.F. (2007). Harnessing high-altitude wind power. *Energy Conversion, IEEE Transactions on*, 22(1), 136–144.

Seifert, J. (2012). A review of the magnus effect in aeronautics. *Progress in Aerospace Sciences*, 55, 17–45. doi:10.1016/j.paerosci.2012.07.001.

Thom, A., Sengupta, S., and Cormack, J. (1933). *Air torque on a cylinder rotating in an air stream*.

White, F.M. (2003). Fluid mechanics. 5th. *Boston: McGraw-Hill Book Company*.

Williams, P., Lansdorp, B., and Ockesl, W. (2008). Optimal crosswind towing and power generation with tethered kites. *Journal of guidance, control, and dynamics*, 31(1), 81–93.